OPTICAL REVIEW Vol. 16, No. 6 (2009) 587–593

Deconvolution of Background-Subtracted Shift-and-Add Image by a Modeled Point-Spread-Function

Susumu KUWAMURA*, Fumiaki TSUMURAYA[1], Makoto SAKAMOTO[1], Noriaki MIURA, and Naoshi BABA[2]

Department of Computer Sciences, Kitami Institute of Technology, 165 Koen-cho, Kitami, Hokkaido 090-8507, Japan
[1]*Nishi-Harima Astronomical Observatory, Sayo, Hyogo 679-5313, Japan*
[2]*Division of Applied Physics, Graduate School of Engineering, Hokkaido University, Sapporo 060-8628, Japan*

(Received March 30, 2009; Accepted August 10, 2009)

Shift-and-add (SAA) is a simple method for celestial speckle imaging. However, the raw SAA-image, a direct output of the SAA operations, is not useful, because a seeing-dependent huge background is superimposed on the high-resolution image of the object. To obtain the latter, a background subtraction (BGS) is applied on the raw SAA-image. The BGS-image so obtained includes negativities due to an over-subtraction that causes brightnesses of the object's image biased downward. The negativity in the BGS-image can be removed by a deconvolution with a point-spread-function (PSF) that has negative values. In this paper, we model the PSF with a shape that possesses peak and concave portions, and perform a deconvolution by iteratively estimating the object's image and the model parameters. The simulated experiment has shown that the present algorithm can restore the object's image with unbiased brightnesses. Processing the observed speckle data of Io (a Jupiter satellite) by the present method has yielded a feasible Io image with reduced negativities.

Keywords: image processing, stellar speckle imaging, shift-and-add, background subtraction, deconvolution, modeled point-spread-function, negativity, Io

1. Introduction

Shift-and-add (SAA)[1)] is a data reduction method for the high-resolution imaging of celestial objects from their atmospherically degraded short-exposure images, or speckle images. In the SAA algorithm, each short-exposure frame is shifted so that the peak (maximum point) of the instantaneous speckled point-spread-function (PSF) is centered, and is added to the SAA-image obtained from the frames that have been similarly processed. A speckle image can be interpreted as a set of randomly translated distorted versions of the diffraction-limited object's image, and the SAA operations average the most intense replicas of the object in the individual frames.[2)] The SAA is a simple algorithm, and has the potential to be operated in real-time as a simple adaptive optics in the visible band.[3)] Since the raw SAA-image (the direct output of the SAA operations) is the first order result of averaging the shifted specklegrams, some additional processes are required to obtain a useful high-resolution image of the object. Efforts to augment and make versatile the SAA method are continuing.

Because the SAA operations are linear, the raw SAA-image $a(\boldsymbol{r})$ can be represented by a convolution of the diffraction-limited object's image $o(\boldsymbol{r})$ and some point-spread-function (PSF) $h(\boldsymbol{r})$,

$$a(\boldsymbol{r}) = o(\boldsymbol{r}) * h(\boldsymbol{r}) \tag{1}$$

("$*$" denotes the convolution operation), provided that the extent of the object is sufficiently small so that the instantaneous PSF due to the atmospheric turbulence is shift-invariant over the object's support.[1)] The PSF of the raw SAA-image (hereafter SAA-PSF), $h(\boldsymbol{r})$, can be considered as a superposition of two parts,[5)] a seeing-dependent broad fog and a compact core. Due to the former part, a huge background is superimposed on the high-resolution object's image in the raw SAA-image.

Subtracting the background[7,11,12)] is the most direct way to extract the high-resolution object's image from the raw SAA-image. The background subtraction (BGS), however, causes negativities of the resultant image due to over-subtraction and the brightnesses biased downward.[13)] Another approach to obtain a background-free image is the deconvolution using data of an unresolvable object (reference) with the Wiener inverse filter,[4,14)] with the CLEAN-algorithm (subtractive deconvolution),[1,2)] with the iterative algorithm,[15)] and so on. This approach requires that the seeing conditions (mainly characterized by the Fried parameter r_0[16)]) under which the object and the reference are observed match, otherwise the image can be damaged by the deconvolution. Hebden *et al.*[17)] have applied the CLEAN-algorithm to background subtracted SAA-images (hereafter BGS-images). The weighted SAA (WSAA) method produces a background-free image[18–21)] without using the reference. However, the WSAA method requires all the object's replicas included in the individual speckle frames to be located. Since these replicas can overlap each other, locating them can be difficult unless the extent of the object is small and/or it has few intense points. Davey *et al.*[14)] have proposed a reference-free blind algorithm, where the zero-and-add technique[22)] is applied on multiple raw SAA-images obtained from different subsets of speckle images.

These previously proposed methods have been demonstrated for a restricted class of objects, where the object has isolated intense points and/or its size is sufficiently small so that its replicas in specklegrams little overlap. As a contrary

*E-mail address: kuwamura@cs.kitami-it.ac.jp

case, there is the application to an object that extends over the frame. Sudo *et al.*[23] have applied the SAA and the self-deconvolution post-processing to a solar imaging.[9] We have previously reported the SAA-imaging results of Io (a Jupiter satellite), where its size is comparable with that of the seeing disk.[13] There, the background is estimated by smoothing the raw SAA-image and is subtracted from the latter. We have applied the BGS to the raw SAA-images of both the object and the reference to minimize the influence of the inconsistency between the seeing conditions, and then deconvolved the object's BGS-image by that of the reference.

Though the BGS can reduce the seeing-dependency of the SAA-PSF, inconsistencies between the BGS-PSFs of images of the object and the reference still remain, and some deconvolutional iterative refinements must follow to absorb these residual inconsistencies. The iterative blind deconvolution algorithm proposed by Ayers and Dainty[24] (AD) can be used for this purpose. However, the AD-algorithm requires both the object and the PSF to be non-negative, and, in principle, cannot be applied to deconvolve a BGS-image, because it must be deconvolved by a PSF possessing negative values. Fortunately, the PSF of the BGS-image can be assumed to have a simple shape, and to be approximated by a peak-concave model representable by a few parameters. In this paper, we propose an approach to deconvolve the BGS-image by a modeled PSF, and verify the method using simulated data. We also report results of the SAA-imaging with the observed speckle data of Io.

2. Principles

2.1 Background subtraction

The background component is estimated by smoothing (low-pass filtering) the raw SAA-image $a(\boldsymbol{r})$, and is subtracted from it. The BGS-image $i(\boldsymbol{r})$ so obtained is then expressed in the Fourier space by

$$I(\boldsymbol{f}) = \{1 - G(\boldsymbol{f})\}A(\boldsymbol{f}), \tag{2}$$

where $\boldsymbol{f}$ is the spatial frequency vector, and an image-space function and its Fourier transform are represented by a lower-case letter and the corresponding upper-case one, respectively. For the smoothing (low-pass) filter $G(\boldsymbol{f})$, we use a Gaussian one

$$G(\boldsymbol{f}) = \exp\left(-\frac{|\boldsymbol{f}|^2}{2w^2}\right), \tag{3}$$

where w represents the width of the Gaussian function. Note that $I(\boldsymbol{0}) = 0$, or equivalently,

$$\iint i(\boldsymbol{r})\, d^2\boldsymbol{r} = 0. \tag{4}$$

2.2 Deconvolution by modeled PSF

The BGS-image $i(\boldsymbol{r})$ can be represented by a convolution of the diffraction-limited object's image $o(\boldsymbol{r})$ and a certain PSF (hereafter, BGS-PSF) $p(\boldsymbol{r})$:

$$i(\boldsymbol{r}) = o(\boldsymbol{r}) * p(\boldsymbol{r}). \tag{5}$$

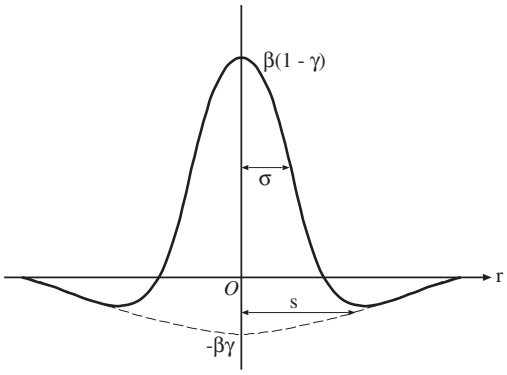

Fig. 1. Profile of the BGS-PSF model. The model parameters to be estimated are β, σ and s. The parameter γ is related to σ and s by eq. (8).

Inspections of the BGS-images of point-like (unresolvable) objects make us conceive a model for the BGS-PSF, the profile of which comprises a peak and a concavity as shown in Fig. 1. Modeling both the peak and the concavity by two Gaussian functions, we have a specific expression for the modeled BGS-PSF $p(\boldsymbol{r};\boldsymbol{\theta})$ with a set of model parameters, $\boldsymbol{\theta}$,

$$p(\boldsymbol{r};\boldsymbol{\theta}) = \beta\left[\exp\left(-\frac{|\boldsymbol{r}|^2}{2\sigma^2}\right) - \gamma\exp\left(-\frac{|\boldsymbol{r}|^2}{2s^2}\right)\right], \tag{6}$$

where σ and s represent the widths of the peak and the concavity, respectively. The zero-integral of $i(\boldsymbol{r})$ as in eq. (4) is attributed to the zero-integral of $p(\boldsymbol{r})$, that is, the modeled PSF must satisfy

$$\iint p(\boldsymbol{r};\boldsymbol{\theta})d^2\boldsymbol{r} = 0 \quad \text{or} \quad P(\boldsymbol{0};\boldsymbol{\theta}) = 0. \tag{7}$$

The model parameters to be estimated are β, σ and s, that is, $\boldsymbol{\theta} = (\sigma, s, \beta)$. Due to the condition of eq. (7), the parameter γ is derived from σ and s by

$$\gamma = \frac{\sigma^2}{s^2}. \tag{8}$$

We have carried out an experiment using the simulated data of a point-like object to verify our PSF-model. Figure 2 shows the radial profiles of the BGS-images obtained using the low-pass filters $G(\boldsymbol{f})$ with various values of w, and demonstrates that the point-response of the SAA/BGS algorithm well fits our PSF-model for any w-value over a wide range.

To obtain the diffraction-limited object's image $o(\boldsymbol{r})$, the BGS-image $i(\boldsymbol{r})$ is deconvolved by the modeled PSF $p(\boldsymbol{r};\boldsymbol{\theta})$ with properly estimated parameters $\boldsymbol{\theta}$. The deconvolution can be performed by the inverse filtering, because the modeled PSF has no zero-points in the Fourier space except at $\boldsymbol{f} = \boldsymbol{0}$. Thus, the Fourier spectrum of the object's image, $O(\boldsymbol{f})$, for $\boldsymbol{f} \neq \boldsymbol{0}$ is given by

$$O(\boldsymbol{f}) = \frac{I(\boldsymbol{f})}{P(\boldsymbol{f};\boldsymbol{\theta})} \quad (\boldsymbol{f} \neq \boldsymbol{0}), \tag{9}$$

where the Fourier transform of the modeled PSF as given by eq. (6) with eq. (8) is

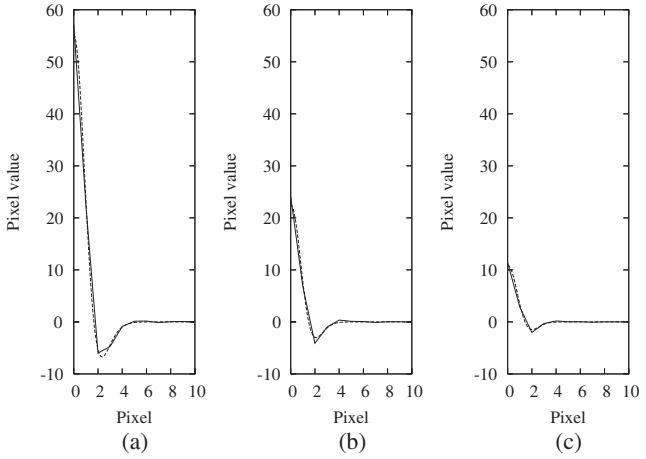

Fig. 2. Radial profiles of the BGS-images of a point-like object as reconstructed from the simulated speckle images are plotted with solid lines. The BGS has been performed using the frequency-domain Gaussian filters with different w-values of (a) 20, (b) 50, and (c) 80% of the cutoff frequency of the telescope's diffraction-limit. The curves of broken lines are the best fit peak-concave models [eq. (6)] to the individual radial profiles. The abscissas of the graphs represent the distance from the center in pixels.

$$P(\boldsymbol{f};\boldsymbol{\theta}) = 2\pi\beta\sigma^2[\exp(-2\pi^2\sigma^2|\boldsymbol{f}|^2) - \exp(-2\pi^2 s^2|\boldsymbol{f}|^2)]. \tag{10}$$

The value of $O(\mathbf{0})$ has to be obtained separately, and can be calculated by

$$O(\mathbf{0}) = \lim_{|\boldsymbol{f}|\to 0}\frac{I(\boldsymbol{f})}{P(\boldsymbol{f};\boldsymbol{\theta})} = A(\mathbf{0})\cdot\lim_{|\boldsymbol{f}|\to 0}\frac{1-G(\boldsymbol{f})}{P(\boldsymbol{f};\boldsymbol{\theta})}, \tag{11}$$

where eq. (2) has been used. The specific form of the limit in eq. (11) can be obtained using eqs. (3) and (10), and invoking the l'Hospital theorem:

$$\lim_{|\boldsymbol{f}|\to 0}\frac{1-G(\boldsymbol{f})}{P(\boldsymbol{f};\boldsymbol{\theta})} = \lim_{|\boldsymbol{f}|\to 0}\frac{-G''(\boldsymbol{f})}{P''(\boldsymbol{f};\boldsymbol{\theta})} = \frac{1}{(2\pi)^3\beta w^2\sigma^2(s^2-\sigma^2)}, \tag{12}$$

where $G''(\boldsymbol{f})$ and $P''(\boldsymbol{f};\boldsymbol{\theta})$ are the second order derivatives with respect to $|\boldsymbol{f}|$ of $G(\boldsymbol{f})$ and $P(\boldsymbol{f};\boldsymbol{\theta})$, respectively.

In the implementation of the algorithm, the image and the Fourier spaces are sampled into $N\times N$ pixels with the sampling intervals of Δr and $\Delta f = (N\Delta r)^{-1}$, respectively. The sampled data-sets of $i(\boldsymbol{r})$ and $I(\boldsymbol{f})$ are denoted by vector notations, $\boldsymbol{i} = \{i_{mn}\}$ and $\boldsymbol{I} = \{I_{kl}\}$, respectively, with i_{mn} and I_{kl} representing the individual sampled data. The two data-sets $\boldsymbol{i}$ and $\boldsymbol{I}$ are related by the discrete Fourier transform (DFT) pair, and there are relationships

$$i_{mn} = i(m\Delta r, n\Delta r), \tag{13}$$

$$I_{kl} = (\Delta f)^2\cdot I(k\Delta f, l\Delta f). \tag{14}$$

Similarly, the discrete versions of the continuous functions $a(\boldsymbol{r})$, $A(\boldsymbol{f})$, $o(\boldsymbol{r})$, $O(\boldsymbol{f})$, $p(\boldsymbol{r};\boldsymbol{\theta})$ and $P(\boldsymbol{f};\boldsymbol{\theta})$ are denoted by vectors (sets of the sampled data) $\boldsymbol{a} = \{a_{mn}\}$, $\boldsymbol{A} = \{A_{kl}\}$, $\boldsymbol{o} = \{o_{mn}\}$, $\boldsymbol{O} = \{O_{kl}\}$, $\boldsymbol{p}(\boldsymbol{\theta}) = \{p_{mn}(\boldsymbol{\theta})\}$, and $\boldsymbol{P}(\boldsymbol{\theta}) = \{P_{kl}(\boldsymbol{\theta})\}$, respectively, where the individual components (sampled data) of each of the vectors are related to the corresponding continuous function by the similar equation of eq. (13) or (14), and two vectors identified by a lower-case letter and its corresponding upper-case letter form a DFT pair.

The flow of the present deconvolution algorithm is shown in Fig. 3. The algorithm is started with the initial estimates of the diffraction-limited object's image $\boldsymbol{o}$ and the PSF-model parameters σ and s. The BGS-image $\boldsymbol{i}$ to be deconvolved may be positionally deviated from the frame center (origin of the coordinate in the image space). This must be corrected before the model fitting, that is, the BGS-image $\boldsymbol{i}$ is properly shifted so that the shifted image has the maximum correlation with the convolution image of the object's estimate $\boldsymbol{o}$ and the modeled PSF $\boldsymbol{p}(\boldsymbol{\theta})$ with $\beta = 1$ (β is a scaling parameter in the ordinate, and its value does not affect the position of the correlation peak). Given the estimates of σ, s, and $\boldsymbol{o}$, the next step is to determine the value of β so as to minimize the sum of square errors,

$$E(\boldsymbol{\theta},\boldsymbol{O}) = \sum_{l=0}^{N-1}\sum_{k=0}^{N-1}|I_{kl} - O_{kl}\cdot P_{kl}(\boldsymbol{\theta})|^2. \tag{15}$$

Such a value of β is found by solving $\partial E/\partial\beta = 0$ for β, and is given by

$$\beta = \frac{\mathrm{Re}\left[\sum_{l=0}^{N-1}\sum_{k=0}^{N-1} I_{kl}\cdot O_{kl}^*\cdot P_{kl}^*(\sigma,s,1)\right]}{\sum_{l=0}^{N-1}\sum_{k=0}^{N-1}|O_{kl}|^2\cdot|P_{kl}(\sigma,s,1)|^2}, \tag{16}$$

where $P_{kl}(\sigma,s,1)$ is $P_{kl}(\boldsymbol{\theta})$ with $\beta = 1$. We have here a complete set of estimates of the PSF-model parameters.

The estimate of the parameter set $\boldsymbol{\theta} = (\sigma, s, \beta)$ can be iteratively refined: for given estimates of β and $\boldsymbol{o}$, the values of σ and s that minimize eq. (15) are searched by the steepest descent or the conjugate gradient algorithm, and the estimates of σ and s are updated by those values. For the updated estimates of σ and s, an estimate of β is calculated by eq. (16) to obtain a refined version of $\boldsymbol{\theta}$. The iteration loop for the parameter refinement is shown as the inner loop in Fig. 3. The refinement is continued until the estimations of the model parameters sufficiently converge.

After the refinement is completed with a fixed BGS-PSF $\boldsymbol{p}(\boldsymbol{\theta})$, the next step is to revise the object's estimate by deconvolving the BGS-image $\boldsymbol{i}$ with $\boldsymbol{p}(\boldsymbol{\theta})$. The direct output, $\boldsymbol{D} = \{D_{kl}\}$, of the deconvolution by the inverse filtering can be written as

$$D_{kl} = \begin{cases} \dfrac{I_{kl}}{P_{kl}(\boldsymbol{\theta})} & (k^2+l^2\neq 0) \\ \dfrac{A_{00}}{(\Delta f)^2}\cdot\lim\limits_{|\boldsymbol{f}|\to 0}\dfrac{1-G(\boldsymbol{f})}{P(\boldsymbol{f};\boldsymbol{\theta})} & (k=l=0) \end{cases}, \tag{17}$$

where the specific value of the limit is given by eq. (12). The result of the inverse filtering, $\boldsymbol{D}$, is a solution of $\boldsymbol{O}$ that minimizes (actually makes zero) the cost function $E(\boldsymbol{\theta},\boldsymbol{O})$ for a given PSF $\boldsymbol{P}(\boldsymbol{\theta})$. The non-negative constraint is then applied on the deconvolved image $\boldsymbol{D}$ in the image space. The non-negative image so obtained is to be the revised

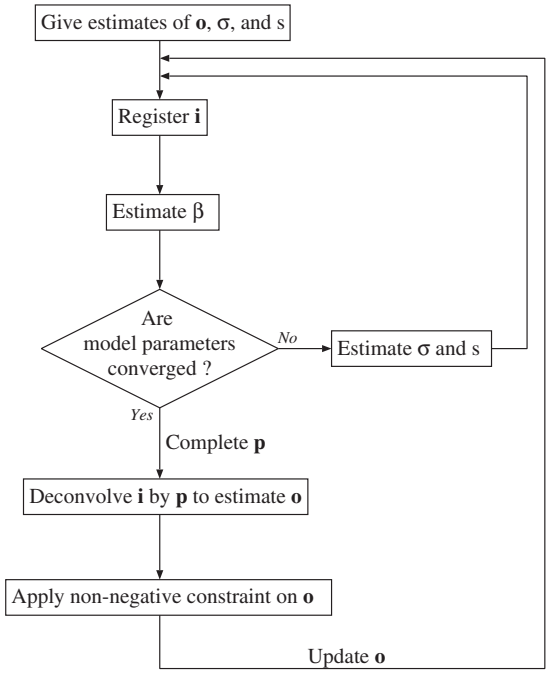

Fig. 3. Algorithm flow of the present deconvolution method. The algorithm is composed of two (inner and outer) loops. The estimates of the PSF-model parameters, β, σ and s, are refined by the inner loop under a fixed object's estimate. For every PSF determined, the object's estimate $\boldsymbol{o}$ is updated, the iteration of which forms the outer loop.

object's estimate $\boldsymbol{O}$. The update of the object's estimate is repeated until it sufficiently converges, which corresponds to iterating the outer loop as in Fig. 3.

3. Experiments and Results

3.1 Simulated data

The present algorithm has been applied to the SAA-image produced from the numerically simulated speckle images of an assumed object as shown in Fig. 4(a). One of the speckle images is shown in Fig. 4(b), where the values of the simulation parameters are summarized in Table 1. Poisson noises have been added to the speckle images. In the data reduction by SAA, we have used a modified algorithm proposed by Gingras and Aruga,[10] where each of the speckle frames is shifted so as to have the maximum correlation with the SAA-image obtained from those similarly processed so far, and is added to it. The SAA-image so obtained is shown in Fig. 4(c), where the 1000 speckle images have been shifted and added. The image after BGS is shown in Fig. 4(d), where 21.6% of the cutoff frequency has been taken for the value of w. In the BGS-image, the object is surrounded by the negative pixels as displayed by a black-level, which are caused by the over-subtraction of the background component.

The deconvolution algorithm as shown in Fig. 3 has been applied to the BGS-image. Figure 4(e) is the resultant object's image $\boldsymbol{o}$ obtained after 10 iterations of the outer loop (10 times updates of the object's estimate) that have been started with the initial object's estimate of a uniform disk

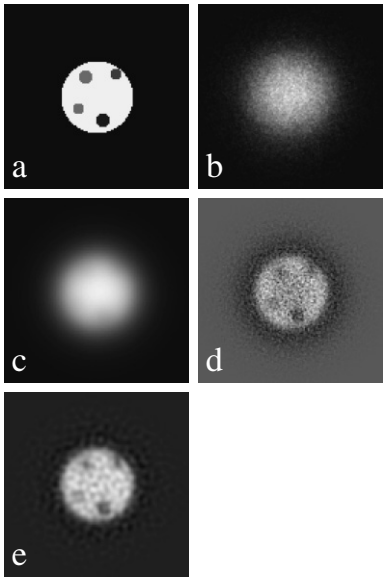

Fig. 4. Images in the simulated experiment. (a) An assumed object. (b) One of the noisy speckle images of the object. (c) The raw SAA-image. (d) The BGS-image. (e) The deconvolved image of (d) by a modeled PSF.

Table 1. Values of the simulation parameters.

Diameter of the telescope aperture (m)	2
F-number of the telescope	12
Magnification	$\times 5$
Wavelength λ (nm)	515
Fried parameter r_0 (cm)	12
Sampling interval Δr (μm)	14
Photon count per frame	1.4×10^5

with a diameter equal to that of the true image. For every object's estimate offered, the PSF-model parameters are iteratively refined until the change rates of the estimated values of σ and s become small. We have iterated the refinement (inner loop) until the relative changes of the parameter estimates become less than 0.05%. The number of times of refinement required for the convergence depends on the initial estimates of the parameters.

In Fig. 5, the cost-function value $E(\boldsymbol{\theta}, \boldsymbol{O})$ and the error of the object's estimate $\boldsymbol{o}$ to the true image $\boldsymbol{t}$ are plotted against the number of iterations of the outer loop, where the error e has been computed by

$$e = \left| \frac{\boldsymbol{o}}{|\boldsymbol{o}|} - \frac{\boldsymbol{t}}{|\boldsymbol{t}|} \right|, \tag{18}$$

which is equivalent to the root-mean-square (RMS) difference between the normalized versions of $\boldsymbol{o}$ and $\boldsymbol{t}$. The changes of the model-parameter estimates as the iteration proceeds are shown in Fig. 6, where the plots are given at each time the refinement is completed. Figures 5 and 6 show that the estimates of the object and the BGS-PSF almost converge after the first few iterations. The number of the outer loop iterations needed for a convergence may vary depending on the initial estimate of the object.

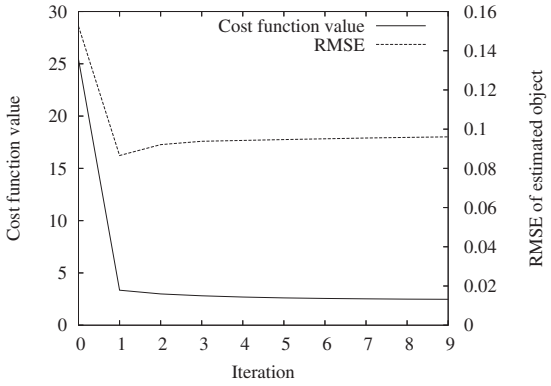

Fig. 5. Value of the cost function $E(\boldsymbol{\theta}, \boldsymbol{O})$ and the RMS error of the estimated object's image are plotted against the number of iterations of the outer loop by a solid line and a broken line, respectively.

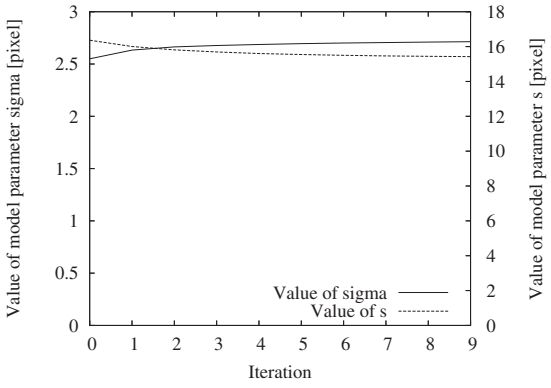

Fig. 6. The estimated values of the model parameters, σ and s, are plotted against the number of iterations of the outer loop by a solid line and a broken line, respectively.

The negativity present in the BGS-image reduces after the deconvolution, which is shown by the profiles in Fig. 7. The power (sum of squared pixel values) of the negative pixels in the BGS-image amounts to 23.5% of the total power, and has been reduced to 0.174% after the deconvolution. A quantitative evaluation for the deconvolved image is shown in Fig. 8, where the average pixel values over the five regions of interest (ROIs) are individually compared with those of the true image. Figure 8 shows a good linearity, implying that the relative values of the pixels well hold in the restored image. A similar graph for the BGS-image before the deconvolution is given in Fig. 9. Comparing Fig. 8 with Fig. 9 shows that the negative bias present in the BGS-image has been eliminated by the deconvolution.

3.2 Observational data

We have applied the present method to the observed speckle images of Io. The observation conditions are summarized in Table 2. The number of speckle frames we have acquired is 1000, which has been limited by the rate of the acquisition system, the term of the seeing condition

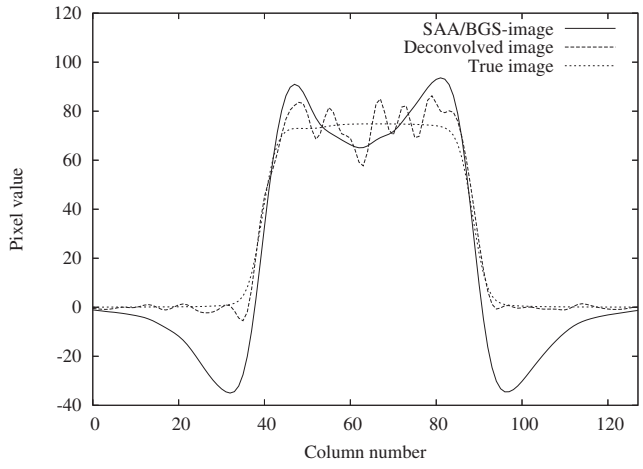

Fig. 7. Profiles of Figs. 4(d) and 4(e), the images before and after the deconvolution, are plotted by a solid and a broken line, respectively, where the profiles have been taken along the horizontal center line of the frame. The profile of the original (true) image is also given by a dotted line.

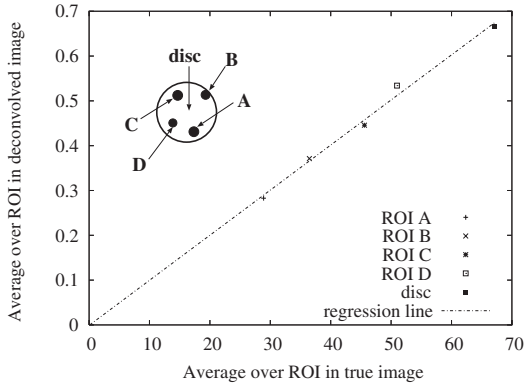

Fig. 8. Pixel values averaged over the individual five ROIs (four circular ones labeled "A", "B", "C", and "D", and the other labeled "disc") in the resulting image of the deconvolution are plotted against those in the true image to graph the reproducibility of the relative pixel values.

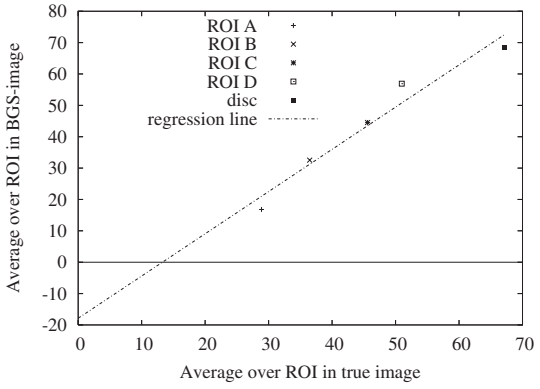

Fig. 9. A graph similar to Fig. 8 is given for the BGS-image (an image before the deconvolution). The negativity present in the BGS-image causes the pixel values to be biased downward.

Table 2. Observation conditions of the speckle data of Io.

Site	Nishi-Harima Astronomical Observatory
Epoch	13:41–13:44 UT, June 7, 2006
Telescope	2m Nayuta telescope (F/12)
Magnification	×5
Wavelength λ (nm)	515
Bandwidth $\Delta\lambda$ (nm)	20
Exposure time (s)	1/30
CCD pixel size Δr (μm)	14

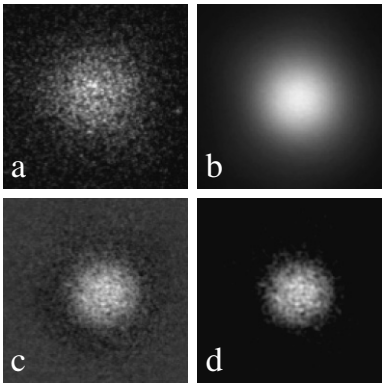

Fig. 10. Results of processing the observational speckle data of Io. (a) One of the speckle images. (b) The raw SAA-image. (c) The BGS-image. (d) The deconvolved image of (c) by a modeled PSF.

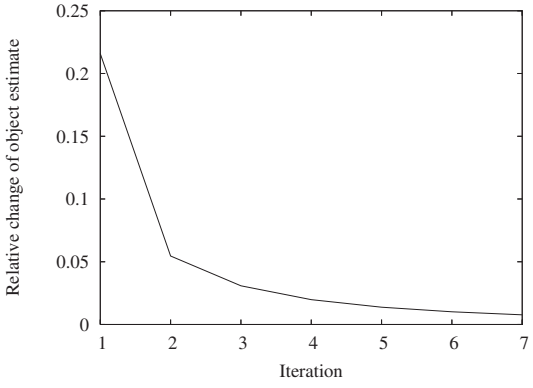

Fig. 11. Relative change of the object's estimate to the previous one is plotted every time the estimate is updated in deconvolution of the BGS-image of Io.

being steady, and the period of the object's image being unchanged (in the present case, determined by Io's rotational speed). Figure 10(a) is one of the 1000 speckle frames acquired, and the raw SAA-image obtained from these frames is shown in Fig. 10(b). Figures 10(c) and 10(d) are the BGS- and the deconvolved images, respectively. As the initial object's estimate for the iterative deconvolution, we have employed a non-negative image obtained by clipping (forcing to be zero) the negative pixels of the BGS-image. The inner loop has been iterated until the relative changes of the parameter estimates reach less than 0.05%. The relative change of the object's estimate to the previous one at each outer loop iteration is plotted in Fig. 11. Correspondingly,

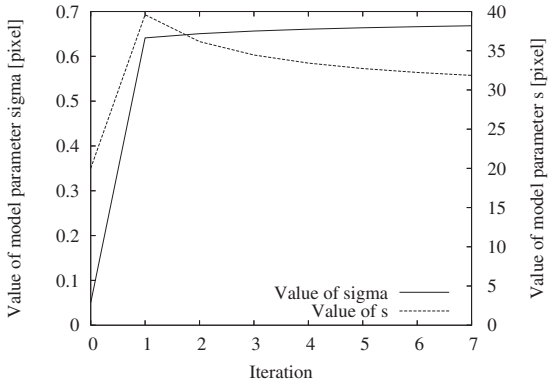

Fig. 12. Estimated values of the model parameters, σ and s, in deconvolution of the BGS-image of Io are plotted against the number of outer loop iterations, where the solid line is for σ and the broken line for s.

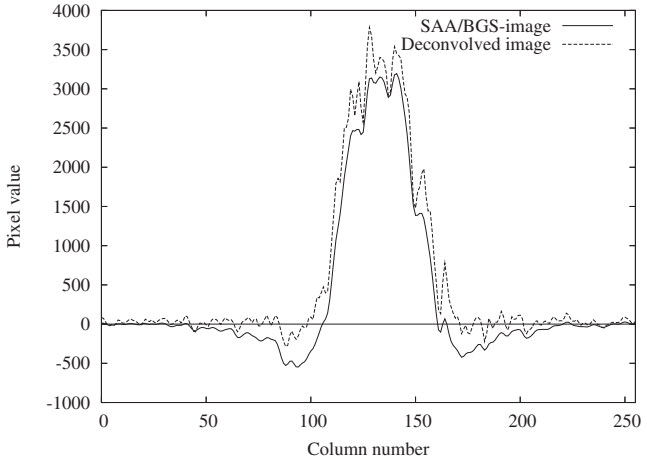

Fig. 13. Profiles of Figs. 10(c) and 10(d), Io's images before and after the deconvolution, are taken along the horizontal center line of the frame, and are plotted by a solid and a broken line, respectively.

the estimated values of the model parameters, σ and s, have varied as shown in Fig. 12. The resultant image of the deconvolution as shown in Fig. 10(d) has been obtained after the object's estimate is updated seven times (after seven iterations of the outer loop), at which the relative change of that estimate has reached less than 1% and the values of the model parameters have almost converged.

The image profiles of Figs. 10(c) and 10(d) are compared in Fig. 13 to show the reduction of the negativity; the negativity has been reduced from 9.58 to 0.522%. The resulting image as in Fig. 10(d) is still noisy. We have applied the non-linear Gaussian edge-preserving filter[25] to denoise the noisy image and to emphasize the significant structures present on Io's surface. The filtered image so obtained is shown in Fig. 14(a). For comparison, a close-up image of the green band taken by the Voyager II spacecraft is given in Fig. 14(b), where the image is of the surface facing the Earth on the observation date, and its scale and the position angle match those of our observational data.

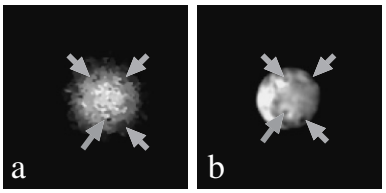

Fig. 14. The deconvolved image shown in Fig. 10(d) is denoised by the non-linear Gaussian filter, and is compared with the image taken by the spacecraft Voyager II. (a) The denoised image of Fig. 10(d). (b) The Voyager's close-up image of Io. The gray arrows in (b) point to the pateras on Io's surface, and those in (a) indicate the dark spots found at the corresponding positions in the restored image.

In Fig. 14(a), there are found significant dark spots at the positions corresponding to those of Io's pateras as indicated in Fig. 14(b). This comparison by the visual inspection rather well verifies our result.

4. Discussion

In our procedure to obtain a feasible object's image from the raw SAA-image, it is once reduced to a zero-mean image by BGS, and then deconvolved by a zero-mean PSF to restore the non-negative object's image. This procedure appears detoured: straightforward is the deconvolution of the raw SAA-image $a(\boldsymbol{r})$ by the SAA-PSF $h(\boldsymbol{r})$ that can be modeled by a "core-fog" model. This model needs essentially three parameters, the widths of the core and the fog parts, and the ratio between the heights of both parts; whereas our peak-concave model has essentially two parameters, σ and s, to be estimated, and the ratio of the concavity depth to the peak height is automatically determined by the zero-mean condition as given by eq. (7). The present algorithm is not a completely blind deconvolution, because it requires an initial estimate of the object. However, the BGS leaves a high-resolution object's image which is fairly feasible except that it has "sunk" to the negative direction, and an object's estimate can be relatively easily obtained from the BGS-image to be deconvolved.

5. Conclusions

We have proposed a deconvolution algorithm to refine the background subtracted SAA-image. This corrects the negativity due to over-subtraction which is unavoidable because of the difficulty in exact identification of the background component. In our algorithm, the alternate estimations of the PSF's model-parameters and the object's image are iterated under the non-negativity constraint on the object, where the model parameters are estimated so as to minimize the cost function as in eq. (15), and the object is estimated by the inverse filtering. The main effect of the deconvolution is to reduce the negativity. This effect has been demonstrated by the experiments using the simulated and the observational speckle data. In the simulated experiment, it has been shown that the negative bias of the BGS-image is effectively eliminated by the deconvolution. The present method can serve as a sophisticated post-processing algorithm in the SAA-imaging.

References

1) R. H. T. Bates and F. M. Cady: Opt. Commun. **32** (1980) 365.
2) R. H. T. Bates: Phys. Rep. **90** (1982) 203.
3) N. Baba, S. Kuwamura, N. Miura, and Y. Norimoto: Opt. Lett. **21** (1996) 626.
4) R. H. T. Bates and B. L. K. Davey: Proc. SPIE **828** (1987) 87.
5) B. R. Hunt, W. R. Fright, and R. H. T. Bates: J. Opt. Soc. Am. **73** (1983) 456.
6) W. G. Bagnuolo, Jr.: Opt. Lett. **10** (1985) 200.
7) A. M. Sinton, B. L. K. Davey, and R. H. T. Bates: J. Opt. Soc. Am. A **3** (1986) 1010.
8) N. Baba, N. Miura, T. Sakurai, K. Ichimoto, D. Soltau, and P. Brandt: Sol. Phys. **188** (1999) 41.
9) Y. Sudo and N. Baba: Opt. Lett. **30** (2005) 1309.
10) D. J. Gingras and T. Aruga: Opt. Lett. **15** (1990) 1380.
11) S. Kuwamura, N. Baba, N. Miura, M. Noguchi, Y. Norimoto, and S. Isobe: Proc. ESO Conf. High-Resolution Imaging by Interferometry II, 1992, p. 461.
12) S. Kuwamura, N. Baba, N. Miura, and E. K. Hege: Astron. J. **105** (1993) 665.
13) S. Kuwamura, F. Tsumuraya, N. Miura, and N. Baba: Publ. Astron. Soc. Pac. **120** (2008) 348.
14) B. L. K. Davey, W. J. Cocke, R. H. T. Bates, D. W. McCarthy, Jr, J. C. Christou, and M. L. Cobb: Astron. J. **98** (1989) 1040.
15) J. C. Christou: Exp. Astron. **2** (1991) 27.
16) J. W. Goodman: *Statistical Optics* (Wiley, New York, 1985) p. 429.
17) J. C. Hebden, J. C. Christou, A. Y. S. Cheng, E. K. Hege, P. A. Strittmatter, J. M. Beckers, and H. P. Murphy: Astron. J. **309** (1986) 745.
18) J. C. Christou, E. K. Hege, J. D. Freeman, and E. Ribak: J. Opt. Soc. Am. A **3** (1986) 204.
19) J. C. Christou, E. Ribak, E. K. Hege, and J. D. Freeman: Opt. Eng. **25** (1986) 724.
20) E. Ribak: J. Opt. Soc. Am. A **3** (1986) 2069.
21) J. C. Christou, J. C. Hebden, and E. K. Hege: Astrophys. J. **327** (1988) 894.
22) B. L. K. Davey, A. M. Sinton, and R. H. T. Bates: Opt. Eng. **25** (1986) 765.
23) Y. Sudo, N. Baba, N. Miura, S. Ueno, and R. Kitai: Appl. Opt. **45** (2006) 2707.
24) G. R. Ayers and J. C. Dainty: Opt. Lett. **13** (1988) 547.
25) V. Aurich and J. Weule: Proc. 17th DAGM-Symp., 1995, p. 538.